Journal of Materials Chemistry A

A novel P2-Na0.6Li0.11Fe0.27Mn0.62O2 cathode with oxygen redox reaction for high-energy Na-ion batteries

Journal:	*Journal of Materials Chemistry A*
Manuscript ID	TA-ART-09-2021-008471.R1
Article Type:	Paper
Date Submitted by the Author:	16-Nov-2021
Complete List of Authors:	Cao, Minghui; East China University of Technology Li, Renyan; East China University of Technology Lin, Shiya; East China University of Technology Zheng, Shaodi; East China University of Technology Ma, Lu; Brookhaven National Laboratory, National Synchrotron Light Source II Tan, Sha; Brookhaven National Laboratory, Chemistry Hu, Enyuan; Brookhaven National Laboratory, Chemistry Shadike, Zulipiya; Shanghai Jiao Tong University Yang, Xiao-Qing; Brookhaven National Laboratory, Chemistry Fu, Zhengwen; Fudan University, Chemistry

ARTICLE

A novel P2-$Na_{0.6}Li_{0.11}Fe_{0.27}Mn_{0.62}O_2$ cathode with oxygen redox reaction for high-energy Na-ion batteries

Received 00th January 20xx,
Accepted 00th January 20xx

DOI: 10.1039/x0xx00000x

Ming-Hui Cao,*[a,b] Ren-Yan Li,[a] Shi-Ya Lin,[a] Shao-Di Zheng,[a] Lu Ma,[c] Sha Tan,[d] Enyuan Hu,[d] Zulipiya Shadike,*[e] Xiao-Qing Yang*[d] and Zheng-Wen Fu*[b]

Owing to the abundance of raw material reserves and low cost, Na-ion batteries (NIBs) have successfully gained widespread attention from academic and industrial communities in the past few decades. However, the insufficient cathode energy density is still one of the critical bottlenecks restricting the development of NIBs. Following a strategy of inducing Li^+ into the transition-metal (TM) layer to enhance the oxygen redox reaction, a novel layered cathode material P2-$Na_{0.6}Li_{0.11}Fe_{0.27}Mn_{0.62}O_2$ (NLFMO) was designed and successfully synthesized. This NLFMO cathode not only delivers a large initial reversible capacity of 207.3 mAh g^{-1}, but also showing a good cyclic performance (104.2 mAh g^{-1} after 80 cycles) and rate capability (126.2 mAh g^{-1} at 1C). The ultrahigh capacity is contributed by both cationic (Fe^{3+}/Fe^{4+}, Mn^{3+}/Mn^{4+}) and partially reversible anionic redox (O^{2-}/O^{n-}) reactions, revealed by *in situ* X-ray absorption spectroscopy (XAS) and X-ray photoelectron spectroscopy (XPS) techniques. Moreover, no detrimental P2-O2 phase transition was observed through *ex situ* X-ray diffraction (XRD) patterns, confirming the high structural stability during Na^+ deintercalation/intercalation processes. These results provide valuable information about the high-energy density layered cathode materials based on anionic redox reaction for NIBs.

Introduction

Na-ion batteries (NIBs), as one of the promising candidates for lithium-ion batteries (LIBs), have been extensively studied for its merits such as abundant Na reserves, low cost and analogous physicochemical properties to Li.[1-6] However, large radius of Na^+ causes structural degradation and slow electrochemical kinetics, which greatly restricts the development of high energy SIBs.[1] Up to now, a large number of new cathode materials for NIBs have been investigated, such as polyanion compounds,[7-10] Prussian blue analogs[11-13] and layered transition-metal oxides[14-16]. Unfortunately, the electrochemical performance is still far from their counterparts for LIBs. Therefore, increasing capacity, extending cycle life and improving the structural stability through rational design and modification of cathode materials promote the market competitiveness of NIBs. From the point of view of electrochemistry and economics, Fe-Mn-based layered oxide, which has abundant reserves and low cost in nature, meet the requirements for sustainable and cost-effective NIBs. Therefore, high-capacity $Na_xFe_yMn_{1-y}O_2$ cathode materials have been widely studied in NIBs.[17-19] Yabuuchi et al.[20] firstly reported the electrochemical performance of P2-$Na_x[Fe_{1/2}Mn_{1/2}]O_2$, which delivered a reversible capacity of about 190 mAh g^{-1} with relatively low average voltage of only 2.75 V based on the Fe^{3+}/Fe^{4+} redox reaction. O3-$NaFe_{1/2}Mn_{1/2}O_2$ provided a reversible capacity of about 100-110 mAh g^{-1} within the potential range of 1.5-4.2 V, but exhibits a serious voltage hysteresis. In recent years, Fe-Mn based multi-transition metal oxides have been also reported for improving the overall performance of cathode materials. Mu et al.[21] synthesized and studied the Na storage performance of O3-$Na_{0.9}[Fe_{0.30}Mn_{0.48}Cu_{0.22}]O_2$, which provided a reversible capacity of about 100 mAh g^{-1} between the voltage range of 2.5-4.1 V and showed a good cycle stability with an average voltage of about 3.2 V. Yabuuchi et al.[22] reported that O3-$Na[Fe_{0.4}Ni_{0.3}Mn_{0.3}]O_2$ provided a reversible capacity of about 140 mAh g^{-1} in the voltage range of 2.0-3.8 V, with an average voltage of about 3 V. In addition, Sun et al.[23] synthesized a series of O3-$Na[Ni_{0.4}Fe_{0.2}Mn_{0.4-x}Ti_x]O_2$ cathode materials and investigated their electrochemical properties. Among them, O3-$Na[Ni_{0.4}Fe_{0.2}Mn_{0.2}Ti_{0.2}]O_2$ (x=0.2) showed excellent cyclic performance with an initial reversible capacity of about 145 mAh g^{-1}. It can be seen that various design and modification strategies have been applied for improving the electrochemical properties of Mn-Fe based cathodes. However, the capacity is still not satisfactory due to the limited charge contribution from the TMs as well as relatively low working potentials.

[a] *Jiangxi Province Key Laboratory of Polymer Micro/Nano Manufacturering and Devices, East China University of Technology, Nanchang, 330013, P. R. China.*
[b] *Shanghai Key Laboratory of Molecular Catalysis and Innovative Materials, Department of Chemistry, Fudan University, Shanghai, 200433, P. R. China*
[c] *National Synchrotron Light Source II, Brookhaven National Laboratory, Upton, NY, 11973, USA*
[d] *Chemistry Division, Brookhaven National Laboratory, Upton, NY, 11973, USA.*
[e] *Institute of Fuel Cells, School of Mechanical Engineering, Shanghai Jiao Tong University, Shanghai, 200240, P. R. China*

Electronic Supplementary Information (ESI) available: ICP-AES results of NLFMO. Rietveld analysis results for NLFMO. Comparison of the electrochemical properties of layered cathode materials for sodium ion batteries based on anionic redox. Average discharge voltage vs. cycle number plot of P2-NLFMO.The charge and discharge voltage profiles with different current rate for P2-NLFMO. Electrochemical performance of NLFMO in the voltage range of 2.0-4.5 V. The capacity contributions of Fe redox, Mn redox and oxygen redox during the initial two cycles. See DOI: 10.1039/x0xx00000x

Since the discovery as an additional capacity source in Li-rich cathode materials, anion redox reaction has attracted enormous attention for further increasing the energy density of battery materials.[24-33] Inspired by this, some P2-type sodium-based cathode materials have been reported to have extraordinary capacity beyond cationic redox reactions.[34-44] However, there are still many unanswered questions about the basic understanding of these systems, such as electrochemical properties, phase evolution in long cycles and capacity fading mechanisms and so on. Here, we explored a novel cathode material P2-$Na_{0.6}Li_{0.11}Fe_{0.27}Mn_{0.62}O_2$ (NLFMO) and tested its electrochemical performance in Na half-cells. This material showed a high initial reversible capacity of 207.3 mAh g^{-1} and maintained a reversible capacity of 104.2 mAh g^{-1} after 80 cycles with an average capacity fade of 0.62% per cycle at 0.1C rate within a wide potential range of 1.5-4.5 V. Moreover, it exhibited a good rate capability achieving a high reversible capacity of 126.2 mAh g^{-1} at current rate of 1C. XPS and *in situ* XAS results confirm that the capacity is contributed by both cationic (Fe^{3+}/Fe^{4+}, Mn^{3+}/Mn^{4+}) and anionic redox(O^{2-}/O^{n-}). Additionally, no undesired P2-O2 phase transition was detected through *ex situ* XRD techniques, suggesting a high degree of structural stability during charging/discharging. These results are quite valuable in guiding the preparation of low cost and high-performance layered cathode materials for NIB.

Experimental

Material synthesis

P2-$Na_{0.6}Li_{0.11}Fe_{0.27}Mn_{0.62}O_2$ was prepared by a traditional solid-state reaction method. A stoichiometric amount of Na_2CO_3, Li_2CO_3, Fe_2O_3 and MnO_2 were ground evenly in an agate mortar and pressed into pellets under a pressure of 15 MPa. Then, the pellets were calcined at 900 °C in O_2 atmosphere for 15 h. As-prepared sample was cooled to room temperature and stored in an Ar-filled glovebox ((H_2O < 0.1 ppm, O_2 < 0.1 ppm) to avoid air exposure.

Material characterization

Synchrotron X-ray diffraction (SXRD) pattern of the P2-$Na_{0.6}Li_{0.11}Fe_{0.27}Mn_{0.62}O_2$ Powder was collected at the BL14B1 beamline of the Shanghai Synchrotron Radiation Facility (SSRF). Cell parameters were derived from Rietveld refinement of the SXRD data obtained by the GSAS software package. The crystal structure of the prepared electrode samples was characterized by XRD on a Bruker D8 Advance diffractometer (Germany) using Cu-Kα radiation within the 2θ angle range between 10° and 70°. The particle morphologies of the samples and the corresponding EDS elemental mappings were evaluated via a scanning electron microscope (SEM, Phenom Prox) equipped with an energy-dispersive X-ray spectroscopic detector. The XPS of the samples was carried out on a PerkinElmer PHI 5000C electron spectrometer using monochromatic Al Kα X-ray source. Binding energies (BEs) of O element in samples were calibrated with respect to the carbon C 1s peak (~284.6 eV). XAS measurements were performed at beamline 7-BM (QAS) of the National Synchrotron Light Sources II (NSLS-II) at Brookhaven National Laboratory (BNL). The XAS spectra were collected with a Si monochromator in transmission mode. Analysis of the XAS data were carried out by using Athena software packages.[45-46]

Electrochemical characterization

The prepared active materials (70 wt %) were mixed with acetylene black (20 wt %) and polyvinylidene fluoride (10 wt %, Sigma-Aldrich) in N-methyl-2-pyrrolidone (NMP). The slurry was coated on Al current collector and dried at 70°C overnight under vacuum. Then the electrode tapes were punched into discs with a diameter of 12mm. The mass loading of the active materials on each working electrode is ~2 mg cm^{-2}. The coin cells (CR2032) were assembled in an Ar-filled glovebox (H_2O < 0.1 ppm, O_2 < 0.1 ppm) using 1.0 M $NaClO_4$ in propylene carbonate (PC) with 5 wt % fluroethylene carbonate (FEC) as the electrolyte. Metallic sodium (Aladdin) served as the counter electrode, and the glass fiber GF/F (Whatman) was used as the separator. The charge and discharge measurements were carried out on Neware battery test system at room temperature. The cyclic voltammetry (CV) measurements at a scan rate of 0.1 mV s^{-1} were performed on a CHI660D electrochemical working station.

Results and discussion

Structure of P2-$Na_{0.6}Li_{0.11}Fe_{0.27}Mn_{0.62}O_2$

A novel Li doped Fe-Mn-based layered compound with chemical formula of $Na_{0.6}Li_{0.11}Fe_{0.27}Mn_{0.62}O_2$ (NLFMO) was successfully prepared by a traditional solid-state method. ICP-AES metal analysis results show that the mole ratio of Na: Li: Fe: Mn is determined to be 0.597:0.108:0.274:0.618 (shown in Table S1 (ESI)). The SXRD pattern shown in Fig. 1a characterizes the long-range structure of the as-synthesized NLFMO Powder. The Rietveld refinement results indicate

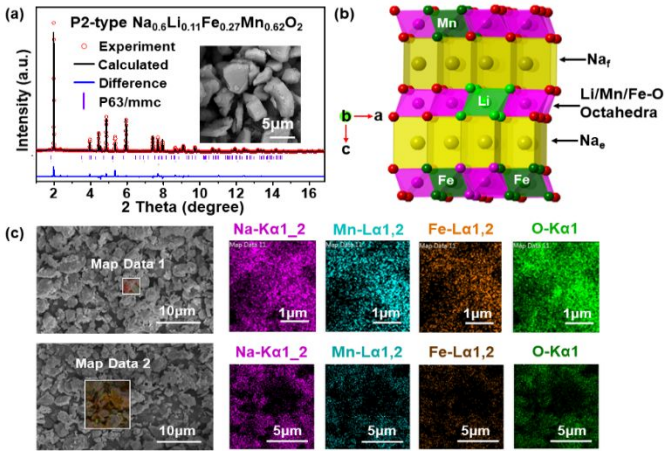

Fig. 1 (a) Rietveld refinement of the SXRD pattern of P2-NLFMO sample. Red circles: experimental, black line: calculated, blue line: difference and magenta bars: Bragg positions (inset: High magnification SEM image of NLFMO). (b) Crystal structure schematic of the P2-NLFMO, legend: yellow (Na), green (Li), magenta (Mn), olive (Fe) and red balls (O). (c) SEM image of NLFMO, and the corresponding EDS elemental mapping of Na (magenta), Mn (cyan), Fe (wine) and O (green), along with the magnified image of the sample (with EDS mapping).

all diffraction peaks of NLFMO can be indexed by a typical P2 structure (space group P63/mmc) without any impurities. The lattice parameters of a=b=2.8420(8) Å, c=10.8722(4) Å and the unit cell volume of V=75.940(2) $Å^3$ are given in Table S2 (ESI). The SEM image shown in the inset of Fig. 1a exhibits that the particle size of the as-prepared sample is in the range of 2-5μm. The EDS mappings were also conducted, revealing that Na (magenta), Mn (cyan), Fe (wine) and O (green) were uniformly distributed in the sample (shown in Fig.

1c). The schematic diagram of the P2-NLFMO based on the refined results is illustrated in Fig. 1b. Within this structure, Na and Li/Mn/Fe atoms are alternately distributed in the oxygen framework, and the hexagonal closest packing is carried out in ABBA...order. Among them, Na^+ with a larger ion radius (1.02 Å) are in prismatic coordination, which behaves as two different types, namely Na_f (sharing face with MO_6) octahedron or Na_e (sharing edge with MO_6). However, Li^+ with smaller radius (0.76 Å) fills the octahedral sites together with the Fe/Mn in the adjacent TM layer.

Electrochemical performance of P2-$Na_{0.6}Li_{0.11}Fe_{0.27}Mn_{0.62}O_2$

The electrochemical properties of P2-$Na_{0.6}Li_{0.11}Fe_{0.27}Mn_{0.62}O_2$ cathode was evaluated in Na-half cells at room temperature. Typical galvanostatic charge/discharge profiles (1st, 2nd, 5th, 10th) at 0.1C (~18 mA g^{-1}) in the voltage range of 1.5-4.5 V are presented in Fig. 2a. It can be observed that the initial charge capacity is ~153.6 mAh g^{-1} with a sloping voltage plateau centered at ~4.2 V, corresponding to ~ 0.55 Na deintercalated per NLFMO. The subsequent initial discharge process yields a specific capacity of 207.3 mAh g^{-1} with an average voltage of ~2.7 V. As summarized in Table S3 (ESI), the as-

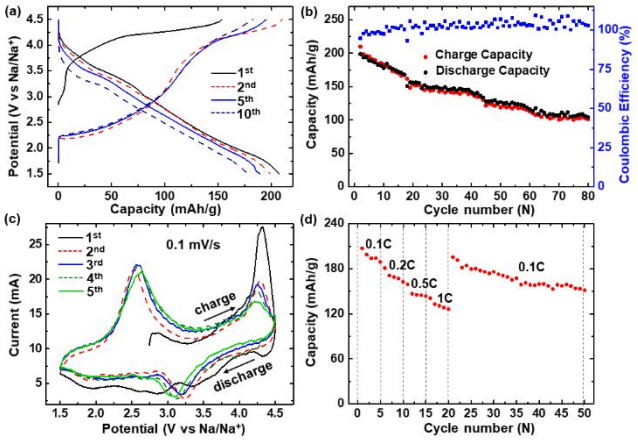

Fig. 2 Electrochemical characterization of NLFMO in Na half-cells: (a) representative charge/discharge curves at 0.1C in the voltage range of 1.5-4.5 V, (b) cyclic voltammogram curves collected within a voltage range of 1.5-4.5 V at a scan rate of 0.1 mV s^{-1}, (c) rate capability (0.1C-1C), (d) charge/discharge capacity and coulombic efficiency as a function of cycle number.

prepared P2-$Na_{0.6}Li_{0.11}Fe_{0.27}Mn_{0.62}O_2$ shows a higher reversible capacity and energy density compared with most of Na layered oxide cathode materials reported previously. This should be attributed to the labile oxygen (lone-pair O) electrons with a linear shape (Na-O-Li) in the higher energy states are oxidized for charge compensation throughout the Na-extraction, thereby increasing the capacity of the material.[24] During the second charge process, the characteristics of the charging curve are very different from the initial one, which includes a long new sloping voltage profile from 2.2 to 4.0 V and a short plateau from 4.0 to 4.5 V. Nevertheless, the shapes of charge and discharge curves in the subsequent cycles coincide well with those in the second cycle. The voltage curves of the second and subsequent cycles show a slope without obvious plateau, indicating that the phase evolution process is dominated by the solid solution reaction. This phenomenon is utterly different from the phase evolution behaviors in the Li-free $Na_xFe_yMn_{1-y}O_2$ ($0 \le y \le 0.5$) cathodes reported before.[17-20] The electrochemical curves of these Li-free materials usually show multiple voltage steps, demonstrating that there are one or more two-phase reactions, which leads to deterioration of electrochemical performance. As shown in Fig. 2a, the NLFMO electrode reveals relatively stable cycle performance with charge/discharge capacities of 210.0/198.9 mAh g^{-1}, 195.1/189.3 mAh g^{-1} and 182.6/178.0 mAh g^{-1} for the 2nd, 5th and 10th cycles, respectively. Furthermore, P2-NLFMO still maintains a reversible capacity of 104.2 mAh g^{-1} after 80 cycles, and the average capacity fade per cycle is 0.62%, which manifests a decent cycle performance after the initial cycle (Fig. 2b). However, the continuing capacity fade and voltage hysteresis (see Fig. S1 (ESI)) over 80 cycles cannot be ignored, which may be ascribed to the irreversible loss of alkali ions from the cathode due to the crystal structure destruction stems from the escape of oxygen.[37-40, 47-48]

The initial five CV curves of the $Na_{0.6}Li_{0.11}Fe_{0.27}Mn_{0.62}O_2$ electrode are shown in Fig. 2c. The sharp anodic peak centered at ~4.2 V associated with oxygen activities in the initial CV profile, corresponding to the extra capacity donated by the oxygen redox reaction.[38-44] The pair of anodic/cathodic peaks in the voltage range of 2-3.5 V in the CV profiles can be assigned to the Mn^{3+}/Mn^{4+} and Fe^{3+}/Fe^{4+} redox process. The CV results above further indicate that the high capacity of the NLMFO is contributed by both transition metal redox reactions and oxygen redox reaction, which is in good agreement with the charge/discharge curves. In addition, the charging and discharging polarization gradually deteriorates with the increased number of cycles, which may be the cause of capacity degradation and voltage hysteresis.

The rate capability of the $Na_{0.6}Li_{0.11}Fe_{0.27}Mn_{0.62}O_2$ electrode is presented in Fig. 2d. The cells were tested by a slow-charge-fast-discharge mode at various discharge rates from 0.1C to 1C while maintaining the charging rate constant at 0.1C. The corresponding charge and discharge voltage curves of P2-NLFMO in Na half-cells at different current rates (0.1C-1C) are shown in Fig. S2 (ESI). Consequently, compared with the initial capacity at 0.1C rate (the final capacity value of 5 cycles under each current rate), the $Na_{0.6}Li_{0.11}Fe_{0.27}Mn_{0.62}O_2$ electrode exhibits good capacity retentions of 91.3%, 78.5%, 69.3% and 60.9% at C/10, C/5, C/2 and 1C rates, respectively. When the current rate is reduced to 0.1C, the $Na_{0.6}Li_{0.11}Fe_{0.27}Mn_{0.62}O_2$ electrode still delivers a reversible capacity of about 195.3 mAh g^{-1}, indicating a good rate capability.

As discussed above, the P2-NLMFO shows a moderate sodium storage performance in the potential range of 1.5-4.5 V. It provides an initial reversible capacity of ~207.3 mAh g^{-1}, which corresponds to 0.74 mol of the Na^+ deintercalated/intercalated from/into the host structure. Moreover, the remarkable capacity should be contributed by both cationic (Fe^{3+}/Fe^{4+}, Mn^{3+}/Mn^{4+}) and anionic redox (O^{2-}/O^{n-}), which will be revealed in the following sections.

For comparison, the electrochemical performance in the voltage range of 2.0-4.5 V is presented in Fig. S3 (ESI), which exhibits better electrochemical performance with relatively stable long-term cyclability (104.9 mAh g^{-1} after 100 cycles with 0.36% for the average capacity fade per cycle) and rate capability (63.1% of initial capacity at 2C). However, the overall performance improvement is at the expense of capacity (165.4 mAh g^{-1} for the initial reversible capacity), which should be closely related to the degree of participation in the

oxygen redox reaction (as the oxygen plateau of the curves is significantly shortened and disappears after the 5th cycle).

Structural evolution upon Na^+ deintercalation/intercalation

The *ex-situ* XRD measurements at different charge/ discharge states were performed to monitor the structural evolution during desodiation/sodiation in the potential range of 1.5-4.5 V at 0.1C (Fig. 3). The XRD patterns of the P2-NLFMO cathode within two theta range of 14° to 17° and 30° to 34° are shown in the purple patches of Fig. 3, corresponding to the clear evolution of the (002) and (004) peaks.

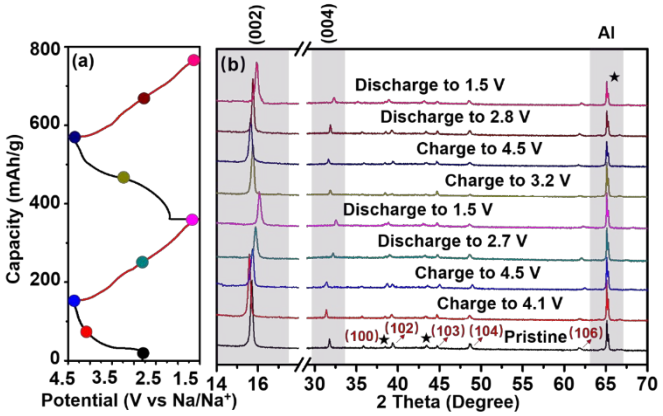

Fig. 3 (a) The initial and second charge-discharge profiles of the Na/NLFMO cell under a current rate of 0.1C at voltage range of 1.5-4.5 V. (b) XRD profiles of the NLFMO cathode cycled to different charge and discharge states, as marked by the colored circles in (a). The asterisks mark the peaks of aluminum foil.

During the initial desodiation process, the (002) and (004) peaks first moved to a lower angle and then slightly shift to a higher angle without new phase formation, suggesting that a solid solution reaction related to *c*-axis expansion/contraction was involved. However, this phenomenon of "*c*-axis shrinkage" is utterly different from the most of common P2-type cathode materials. This can be attributed to the slight sliding of the TMO_2 layer to mitigate the increased electrostatic repulsion between them, resulting in the formation of a secondary P2 phase with shortened *c* lattice parameter. Similar phenomena were also observed in some other P2-type layered compounds in the high-voltage phase transitions region.[49-50] Although the intensity of (100), (102), (103), (104) and (106) peaks are too weak to be detected, it can still be seen that they move towards high angles after charging. During the initial sodiation process, XRD pattern of P2-NLFMO underwent an almost completely opposite phase transition pathway, indicating the structural reversibility over the first cycle. During the second desodiation process, the (002) and (004) peaks significantly moved to a lower two-theta angle, resulting in a larger layer spacing, which can account for the fact that the second charge capacity is as high as 210.0 mAh g^{-1}. Additionally, the (002) and (004) peaks almost return to the pristine state after second cycle, further indicating a high structural reversibility during subsequent cycles.

These results demonstrated that the NLFMO cathode always maintains the P2 phase during the charge/discharge processes, and no new phase is generated within wide voltage range except for the shift of the peak position and the change of the peak intensity. Even charged to high voltage of 4.5 V, no notable sign of the O2 or OP4 phase was observed, which was commonly reported in previous literature.[51-53] In addition, unlike Na_xMnO_2 or $Na_xFe_yMn_{1-y}O_2$,[53-57] no obvious splitting of the (00l) peak was observed when discharging to 1.5 V, which further proves that no P2' phase was involved in the deep discharge state. Note that the presence of monovalent Li ions in the TM layers allows more Na ions to reside in the prismatic sites, stabilizing the overall charge balance of the compound. Consequently, more Na ions remain in the compound upon charge, the P2 structure is retained in the high voltage region, and the phase transformation is delayed. In addition, the suppressed P2/O2 phase transition makes the electrochemical curves smoother.

To check the structural changes more intuitively, the cell parameters (*a*, *b*, *c*, *V*) at various charge/discharge states calculated from the ex-XRD results of NLFMO are demonstrated in Fig. 4. The unit-cell volume changes before and after the first/second Na^+ deintercalation were calculated as ~3.48% and ~1.30% (see Fig. 4), respectively, and the latter is very close to zero-strain characteristics.[58-59] Additionally, the unit-cell volume change after the second cycle is significantly smaller than that of the first cycle, indicating that the material exhibits better reversibility during the second cycle.

Since the overall crystal structure is relatively robust against the irreversible structural change caused by the large amount of Na^+ insertion/extraction, the P2-NLFMO exhibits good cycle reversibility with ultrahigh capacities for the initial two cycles. However, the non-negligible capacity decay and voltage hysteresis during discharge may be mainly attributed to two factors: (1) TM migration, structural distortion and stacking faults caused by the accumulated irreversible

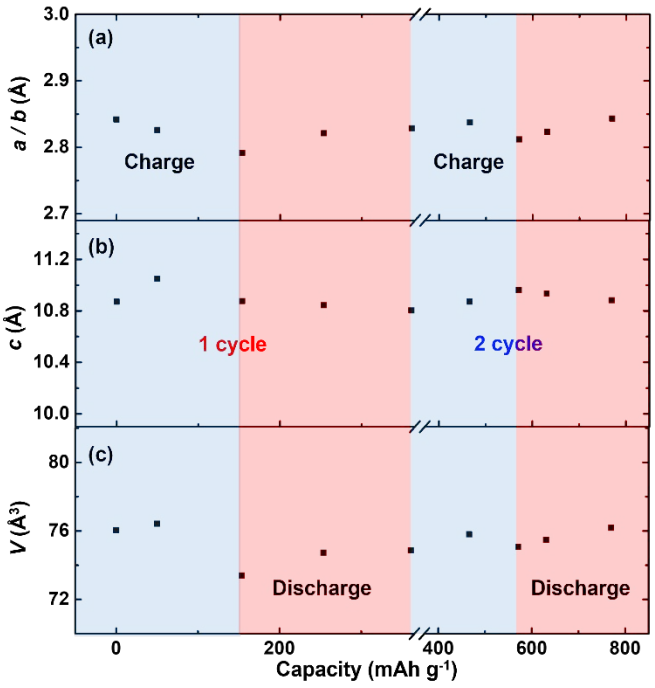

Fig. 4 (a) Lattice parameters of a/b in hexagonal crystal at different charge/discharge states calculated from the ex-XRD results. (b) Lattice parameters of c in hexagonal crystal at different charge/discharge states calculated from the ex-XRD results. (c) Unit cell volume (V) of NLFMO during charge and discharge.

lattice oxygen loss. (2) the formation of amorphous phase peroxides (undetectable in XRD) that grow with cycling. [60]

In situ X-ray absorption spectroscopy (XAS) characterization

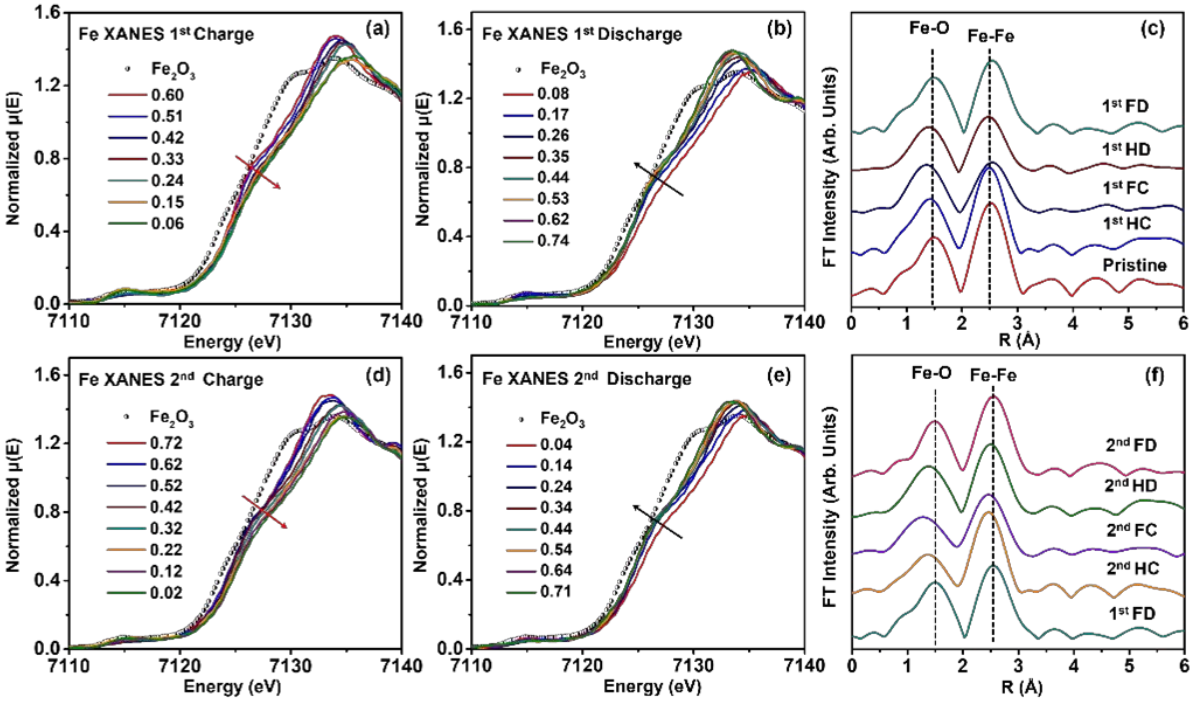

Fig. 5 (a), (b), (d) and (e) Normalized XANES spectra of NLFMO at Fe K-edge at various states during the first and second charge/discharge processes in the voltage range of 1.5-4.5 V, respectively. (c) and (f) Corresponding Fourier transform X-ray absorption near-edge structure (XANES) spectra at Fe K-edges of NLFMO electrodes during the initial and second cycles (HC: half-charged, FC: fully-charged, HD: half-discharged, FD: fully-discharged).

To study the changes in the local structure and valence state of P2-NLFMO, the *in situ* XAS data at Fe and Mn K-edges were collected during the initial and second cycle, as shown in Fig. 5 and 6, respectively. By comparing with the standard reference compounds, the average valence states of Fe and Mn ions in the as-prepared NLFMO can be estimated as 3+ and 4+, respectively.

For the Fe K-edge X-ray absorption near edge structure (XANES) spectroscopy (Fig. 5a) in the initial cycle, an obvious shift of the position of the absorption edge to higher energy can be seen during charge, while the opposite change of the absorption edge position to a lower energy was observed during discharge (Fig. 5b). By comparing with the Fe K-edge XAS spectra of standard reference compounds, the valence state of Fe can be determined at a state between 3+ and 4+ after full charge and at 3+ after discharge. Note that it can be inferred from the XANES result analysis that the $Fe^{3+}/Fe^{3+\sim4+}$ redox contributed the same capacity of ~67 mAh g^{-1} during the initial charge and discharge process, which is also consistent with the characteristics of the first charge-discharge curve. During the second charging/discharging process (Fig. 5d-f), Fe K-edge XAS spectra and FT-EXAFS show similar trend in peak shifting as the initial cycle. It should be noted that, Fe K-edge energy of the second charging state is obviously higher than that of the initial charging, indicating that Fe contributes more capacity (~76.5 mAh g^{-1}) during the second cycle.

The valence change of Mn during cycling was also investigated. As expected, the absorption edge of Mn keeps unchanged during the first desodiation process (Fig. 6a), indicating that Mn did not involve in charge compensation during the initial charging. Combined with the valence change of Fe ion, it can be inferred that oxygen redox have contributed to a considerable capacity of ~86 mAh g^{-1} in the initial charge process. However, the FT-EXAFS (Fig. 6c) shows shortened Mn-O bonding after the initial charging, which could be contributed by the local environment change around Mn. It has been revealed in other Mn-based P2-type layered oxides that the oxygen can also participate the charge compensation within higher voltage region, thus the structural change around the Mn is possibly induced by the oxygen redox. It can be clearly seen that Mn^{4+} was reduced to $Mn^{3+\sim4+}$ after the first discharge process (Fig. 6b), corresponding a capacity contribution of ~86.75 mAh/g. Combined with the valence change of Fe ion, it can be inferred that the capacity contributed by oxygen redox reduced to ~53 mAh g^{-1} in the initial discharge process, which could be attributed to the lattice oxygen loss caused by the irreversible escape of oxygen. During the second charge processes (Fig. 6d-e), the Mn K-edge absorption energy moved rigidly to higher position, very close to the absorption edge of the MnO_2, implying that the average valence state of Mn ions in NLFMO can be estimated to be ~4+. During the second discharge processes (Fig. 6d), valence of Mn^{4+} reduced to $Mn^{3+\sim4+}$ again, indicating high reversibility of Mn during the electrochemical cycles. It should be noted that the capacity contributed by $Mn^{4+}/Mn^{3+\sim4+}$ during the second charge and discharge process is the same as that during the initial discharge process. This also indirectly confirms that the capacities contributed by O^{2-}/O_2^{n-} redox during the second charge and discharge process are 47 and 36 mAh g^{-1}, respectively. The decrease in the capacity contributed by oxygen redox may be due to the formation of an amorphous phase peroxide that grows with the cycle.[60] As expected, the Mn-O bond length changes significantly in the first discharge process and second charge/discharge processes (Fig. 6c, f), which is consistent with the XANES results. Moreover, nonexistence of Mn^{3+}

inhibit the inverse side reaction,[61-66] which guarantees the structural stability.

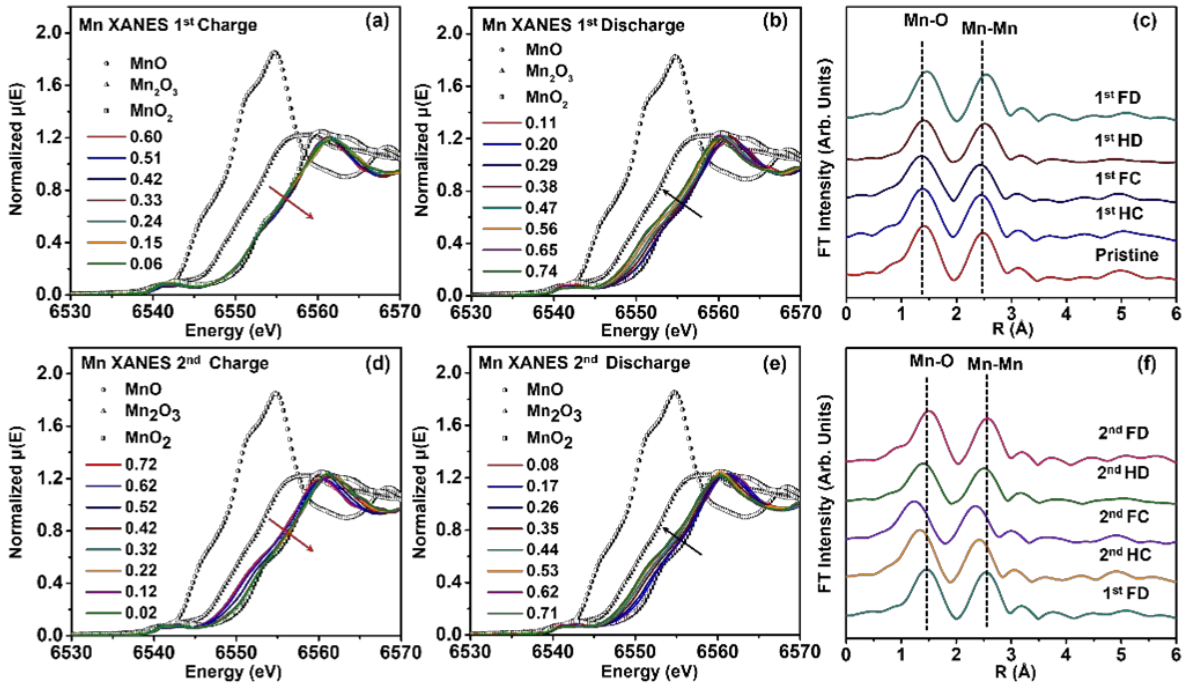

Fig. 6 (a), (b), (d) and (e) Normalized XANES spectra of NLFMO at Mn K-edge at various states during the first and second charge/discharge processes in the voltage range of 1.5-4.5 V, respectively. (c) and (f) Corresponding Fourier transform X-ray absorption near-edge structure (XANES) spectra at Mn K-edges of NLFMO electrodes during the initial and second cycles (HC: half-charged, FC: fully-charged, HD: half-discharged, FD: fully-discharged).

In order to make capacity attribution assignment more intuitive, the contribution of Fe, Mn and O redox capacities in the first and second cycles through careful analysis of in-situ XAS were quantified and shown in Fig. S4 (ESI). The results above indicate that both Fe and Mn ions exhibit strong electrochemical reaction activity during the charging/discharging processes (except for the first charge process). Nevertheless, the high initial charging capacity (153 mAh g^{-1}) and discharge capacity (~207-210 mAh g^{-1}) of the NLFMO apparently cannot be fully explained by the transition-metal redox reactions. The exploration of oxygen redox will be further illustrated as following part.

Exploration of anionic redox reaction mechanism

To investigate anionic redox activity during electrochemical processes, the XPS experiments were performed on the P2-NLFMO electrode at the first and second charged/discharged states as shown in Fig. 7. The characteristic peak of O^{2-} anions at ~529.5 eV in the original NLFMO sample should be assigned to the crystalline network (Fig. 7a). When charged to 4.5 V, a new peak (~530.5 eV) appears, which can be attributed to the formation of $(O_2)^{n-}$ substances due to presence of oxygen redox reaction in high-voltage region (Fig. 7b).[67-68] In addition, there is another new peak belonging to the oxygenated deposited species, which are produced by the common side reactions of electrolyte under high voltage. As expected, the peak in the O1s spectrum disappears after discharge, indicating that $(O_2)^{n-}$ species are reduced to O^{2-} again (Fig. 7c). When recharged to 4.5 V after a full cycle, the peak corresponding to oxygen redox reaction emerges again but degraded, indicating the reduction of the oxygen activity (Fig. 7d). However, after the second cycle, the peak disappears and the O1s spectrum returns to the initial discharged state, further demonstrating that the anionic redox process is partially reversible (Fig. 7e). In conclusion, during the initial and second cycle, the reversible anionic redox process (O^{2-}/O_2^{n-}) have been validated in the NLFMO electrode.

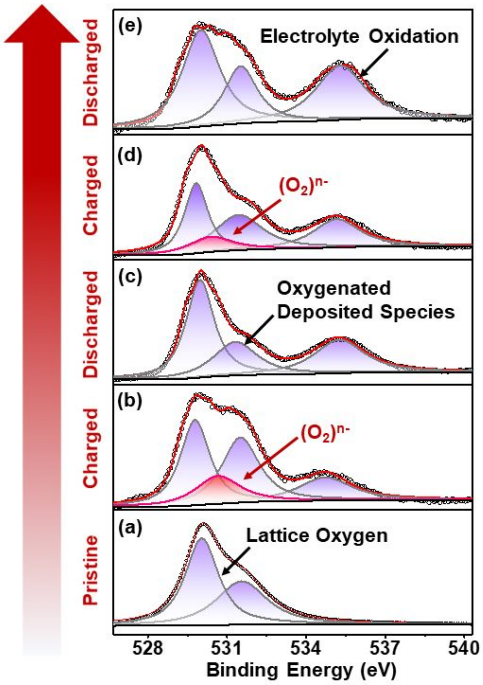

Fig. 7 O 1s XPS spectra collected from NLFMO cathodes at (a) pristine, (b) 1st charged, (c) 1st discharged, (d) 2nd charged and (e) 2nd discharged states, respectively.

Conclusions

P2-$Na_{0.6}Li_{0.11}Fe_{0.27}Mn_{0.62}O_2$ as a new cathode material has been synthesized by a traditional solid-state method. The NLFMO electrode not only provides a high initial reversible capacity of 207.3 mAh g^{-1}, but also a good rate capability (126.2 mAh g^{-1} at 1C) and cycle performance (104.2 mAh g^{-1} after 80 cycles). *Ex-situ* XRD results revealed that Li substitution of Fe in NLMFO exhibits a phase evolution process dominated by solid solution reaction, which greatly improved electrochemical performance and the structural reversibility of the electrode. *In situ* XAS and XPS results demonstrated the high capacity is contributed by Fe^{3+}/Fe^{4+}, Mn^{3+}/Mn^{4+} and the partially reversible O^{2-}/O_2^{n-}. The extraordinary capacity of NLFMO proves the effectiveness of Li doping in inducing oxygen redox reactions, and lays an experimental and theoretical foundation for the design of more high-performance layered oxide cathodes with reversible anionic redox reactions. However, the excessive oxygen oxidation during charging causes irreversible electrochemical reaction processes. As the cycle number increases, the accumulated irreversible lattice oxygen loss may trigger detrimental TM migration, structure distortion and stack faults, leading to capacity decay, voltage fade, poor cycling stability and sluggish Na^+ deintercalation/intercalation kinetics. Therefore, effective approaches for improving the cyclic stability of NLFMO cathode should be considered in the future.

Conflicts of interest

There are no conflicts to declare.

Acknowledgements

We thank financial support by the National Natural Science Foundation of China (Grant No. 22005047), Shanghai Science and Technology Committee (Grant 19DZ2270100), the Opening Project of Jiangxi Province Key Laboratory of Polymer Micro/Nano Manufacturing and Devices (Grant PMND201909) , the Doctoral Scientific Research Foundation of East China University of Technology (Grant DHBK2019121), 2021 Jiangxi Province Innovation and Entrepreneurship Training Program for College Students (Grant S202110405024). The work at Brookhaven National Laboratory was supported by the Assistant Secretary for Energy Efficiency and Renewable Energy, Vehicle Technology Office of the U.S. Department of Energy through the Advanced Battery Materials Research (BMR) Program under contract DE-SC0012704. This research used resources at beamlines 7-BM (QAS) of the National Synchrotron Light Source II, a U.S. Department of Energy (DOE) Office of Science User Facility operated for the DOE Office of Science by Brookhaven National Laboratory under Contract No. DE-SC0012704. We would also like to thank beamline BL14B1 of the Shanghai Synchrotron Radiation Facility (SSRF).

Notes and references

1 B. L. Ellis and L. F. Nazar, *Curr. Opin. Solid State Mater. Sci.*, 2012, **16**, 168-177.
2 M. D. Slater, D. Kim, E. Lee and C. S. Johnson, *Adv. Funct. Mater.*, 2013, **23**, 947-958.
3 S. -W. Kim, D. -H. Seo, X. Ma, G. Ceder and K. Kang, *Adv. Energy Mater.*, 2012, **2**, 710-721.
4 S. Y. Hong, Y. Kim, Y. Park, A. Choi, N. -S. Choi and K. T. Lee, *Energy Environ. Sci.*, 2013, **6**, 2067.
5 H. -J. Liang, B. -H. Hou, W. -H. Li, Q. -L. Ning, X. Yang, Z. -Y. Gu, X. -J. Nie, G. Wang and X. -L. Wu, *Energy Environ. Sci.*, 2019, **12**: 3575-3584.
6 B. -H. Hou, Y. -Y. Wang, Q. -L. Ning, W.-H. Li, X.-T. Xi, X. Yang, H.-J. Liang, X. Feng, and X. –L. Wu, *Adv. Mater.*, 2019, **31**, 1903125.
7 Z. -Y. Gu, J. -Z. Guo, X. -X. Zhao, X. -T. Wang, D. Xie, Z. -H. Sun, C. -D. Zhao, H. -J. Liang, W. –H. Li, X. -L. Wu, *InfoMat.*, 2021, **3**: 694.
8 B. L. Ellis, W. R. M. Makahnouk, Y. Makimura, K. Toghill, L. F. Nazar, *Nature Mater.*, 2007, **6**, 749-753.
9 P. Barpanda, T. Ye, M. Avdeev, S. -C. Chung and A. Yamada, *J. Mater. Chem. A*, 2013, **1**, 4194-4197.
10 M. Nose, H. Nakayama, K. Nobuhara, H. Yamaguchi, S. Nakanishi and H. Iba, *J. Power Sources*, 2013, **234**, 175-179.
11 H. Yi, R. Qin, S. Ding, Y. Wang, S. Li, Q. Zhao and F. Pan, *Adv. Funct. Mater.*, 2021, **31**, 2006970.
12 C. Wei, X. Y. Fu, L. L. Zhang, J. Liu, P. P. Sun, L. Gao, K. J. Chang and X. L. Yang, *Chem. Eng. J.*, 2021, **421**, 127760.
13 Q. Liu, Z. Hu, M. Chen, C. Zou, H. Jin, S. Wang, S. Chou, Y. Liu, and S. Dou, *Adv. Funct. Mater.*, 2020, **30**, 1909530.
14 A. Caballero, L. Hernan, J. Morales, L. Sanchez, J. Santos Pena and M. A. G. Aranda, *J. Mater. Chem.*, 2002, **12**, 1142-1147.
15 R. Berthelot, D. Carlier and C. Delmas, *Nature Mater.*, 2011, **10**, 74-80.
16 M. Guignard, C. Didier, J. Darriet, P. Bordet, E. Elkaïm and C. Delmas, *Nature Mater.*, 2013, **12**, 74-80.
17 J. S. Thorne, R. A. Dunlap and M. N. Obrovac, *J. Electrochem. Soc.*, 2012, **160**, A361-A367.
18 B. Mortemard de Boisse, D. Carlier, M. Guignard and C. Delmas, *J. Electrochem. Soc.*, 2013, **160**, A569-A574.
19 M. Yoncheva, R. Stoyanova, E. Zhecheva, E. Kuzmanova, M. Sendova-Vassileva, D. Nihtianova, D. Carlier, M. Guignard and C. Delmas, *J. Mater. Chem.*, 2012, **22**, 23418.
20 N. Yabuuchi, M. Kajiyama, J. Iwatate, H. Nishikawa, S. Hitomi, R. Okuyama, R. Usui, Y. Yamada and S. Komaba, *Nature Mater.*, 2012, **11**(6), 512-517.
21 L. Mu, S. Xu, Y. Li, Y. S. Hu, H. Li, L. Chen and X. Huang, *Adv. Mater.*, 2015, **27**, 6928-6933.
22 N. Yabuuchi, M. Yano, H. Yoshida, S. Kuze, S. Komaba, *J. Electrochem. Soc.*, 2013, 160, A3131-A3137.
23 X. Sun, Y. Jin, C. Y. Zhang, J. W. Wen, Y. Shao, Y. Zang and C. H. Chen, *J. Mater. Chem. A*, 2014, **2**, 17268-17271.
24 C. Zhao, Q. Wang, Y. Lu, Y. S. Hu, B. Li and L. Chen, *J. Phys. D: Appl. Phys.*, 2017, **50**, 183001.
25 K. Luo, M. R. Roberts, R. Hao, N. Guerrini, D. M. Pickup, Y. Liu, K. Edström, J. Guo, A. V. Chadwick, L. C. Duda and P. G. Bruce, *Nature Chem.*, 2016, **8**, 684-691.
26 C. Zhao, Q. Wang, Y. Lu, Y. S. Hu, B. Li and L. Chen, *J. Phys. D: Appl. Phys.*, 2017, **50**, 183001.
27 N. Yabuuchi, M. Takeuchi and M. Nakayama, *Proc. Natl. Acad. Sci.*, 2015, **112**, 7650-7655.
28 C. Zhan, Z. Yao, J. Lu, L. Ma, V. A. Maroni, L. Li, E. Lee, E. E. Alp, T. Wu, J. Wen, Y. Ren, C. Johnson, M. M. Thackeray, M. K. Y. Chan, C. Wolverton and K. Amine, *Nat. Energy*, 2017, **2**, 963-971.
29 M. Sathiya, A. M. Abakumov, D. Foix, G. Rousse, K. Ramesha, M. Saubanère, M. L. Doublet, H. Vezin, C. P. Laisa, A. S. Prakash, D. Gonbeau, G. VanTendeloo and J. -M. Tarascon, *Nature Mater.*, 2015, **14**, 230-238.

30 E. McCalla, A. M. Abakumov, M. Saubanère, D. Foix, E. Berg, G. Rousse, M. -L. Doublet, D. Gonbeau, P. Novak, G. Tendeloo, R. Dominko and J. -M. Tarascon, *Science*, 2015, **350**, 1516-1521.
31 B. M. De Boisse, G. Liu, J. Ma, S. -I. Nishimura, S. -C. Chung, H. Kiuchi, Y. Harada, J. Kikkawa, Y. Kobayashi, M. Okubo and A. Yamada, *Nat. Commun.*, 2016, **7**, 11397.
32 A. J. Perez, D. Batuk and M. Saubanère, G. Rousse, D. Foix, E. McCalla, E. J. Berg, R. Dugas, K. H. W. van den Bos, M. -L. Doublet, D. Gonbeau, A. M. Abakumov, G. V. Tendeloo and J. -M. Tarascon, *Chem. Mater.*, 2016, **28**, 8278-8288.
33 Y. Qiao, S. Guo, K. Zhu, P. Liu, X. Li, K. -Z. Jiang, C. -J. Sun, M. W. Chen and H. -S. Zhou, *Energy Environ. Sci.*, 2018, **11**, 299-305.
34 U. Maitra, R. A. House, J. W. Somerville, N. Tapia-Ruiza, J. G. Lozanoa, N. Guerrinia, R. Hao, K. Luo, L. Jin, M. A. Pérez-Osorioa, F. Masselc, D. M. Pickup, S. Ramos, X. Lue, D. E. McNallye, A. V. Chadwick, F. Giustinoa, T. Schmitte, L. C. Duda, M. R. Roberts and P. G. Bruce, *Nature Chem.*, 2018, **10**, 288.
35 X. Bai, M. Sathiya, B. Mendoza-Sánchez, A. Iadecola, J. Vergnet, R. Dedryvère, M. Saubanère, A. M. Abakumov, P. Rozier and J. -M. Tarascon, *Adv. Energy Mater.*, 2018, **8**, 1802379.
36 C. Ma, J. Alvarado, J. Xu, R. J. Clément, M. Kodur, W. Tong, C. P. Grey and Y. S. Meng, *J. Am. Chem. Soc.*, 2017, **139**, 4835-4845.
37 Y. Li, X. Wang, Y. Gao, Q. Zhang, G. Tan, Q. Kong, S. M. Bak, G. Lu, X. -Q. Yang, L. Gu, J. Lu, K. Amine, Z. X. Wang and L. Chen, Native Vacancy Enhanced Oxygen Redox Reversibility and Structural Robustness, *Adv. Energy Mater.*, 2019, **9**, 1803087.
38 Z. Shadike, Y. N. Zhou, L. L. Chen, Q. Wu, J. L. Yue, J. N. Zhang, X. -Q. Yang, L. Gu, X. -S. Liu, S. -Q. Shi and Z. W. Fu, *Nat. Commun.*, 2017, **8**, 566.
39 T. Wang, G. X. Ren, Z. Shadike, J. L. Yue, M. H. Cao, J. N. Zhang, M. -W. Chen, X. -Q. Yang, S. -M. Bak, P. Northrup, P. Liu, X. -S. Liu and Z. W. Fu, *Nat. Commun.*, 2019, **10**, 1-12.
40 N. Yabuuchi, R. Hara, M. Kajiyama, K. Kubota, T. Ishigaki, T. Hoshikawa and S. Komaba, *Adv. Energy Mater.*, 2014, **4**, 1301453.
41 Y. -J. Guo, P. -F. Wang, Y. -B. Niu, X. -D. Zhang, Q. H. Li, X. Q. Yu, M. Fan, W. -P. Chen, Y. Yu, X. F. Liu, Q. H. Meng, S. Xin, Y. -X. Yin and Y. -G. Guo. *Nat. Commun.*, 2021, **12**: 1-11.
42 X. Rong, J. Liu, E. Hu, Y. Liu, Y. Wang, J. Wu, X. Yu, K. Page, Y. -S. Hu, W. Yang, H. Li, X. -Q Yang, L. -Q. Chen and X. Huang, *Joule*, 2018, **2**: 125-140.
43 X. Rong, E. Hu, Y. Lu, F. Meng, C. Zhao, X. Wang, Q. Zhang, X. Yu, L. Gu, Y. -S. Hu, H. Li, X. Huang, X. -Q. Yang, C. Delmas and L. Q. Chen, *Joule*, 2019, **3**: 503-517.
44 C. Zhao, Z. Yao, J. Wang, Y. Lu, X. Bai, A. Aspuru-Guzik, L. Q. Chen and Y. -S. Hu, *Chem*, 2019, **5**(11), 2913-2925.
45 M. Newville, *J. Synchrotron Radiat.*, 2001, **8**, 322-324.
46 B. Ravel and M. Newville, *J. Synchrotron Radiat.*, 2005, **12,** 537-541.
47 W. Li, A. Dolocan, P. Oh, H. Celio, S. Park, J. Cho and A. Manthiram, *Nat. Commun.*, 2017, **8**, 1-10.
48 J. N. Zhang, Q. Li, Y. Wang, J. Zheng, X. Yu and H. Li, *Energy Storage Mater.*, 2018, **14**, 1-7.
49 N. Yabuuchi, R. Hara, M. Kajiyama, K. Kubota, T. Ishigaki, A. Hoshikawa and S. Komaba, *Adv. Energy Mater.*, 2014, **4**, 1301453.
50 L. Yang, X. Li, J. Liu, S. Xiong, X. Ma, P. Liu, J. Bai, W. Xu, Y. Tang, Y. -Y. Hu, M. Liu and H. Chen, *J. Am. Chem. Soc.*, 2019, **141**, 6680-6689.
51 Z. Lu and J. R. Dahn, *J. Electrochem. Soc.*, 2001, **148**, A1225.
52 E. Talaie, V. Duffort, H. L. Smith, B. Fultz and L. F. Nazar, *Energy Environ. Sci.*, 2015, **8**, 2512-2523.
53 N. Yabuuchi, M. Kajiyama, J. Iwatate, H. Nishikawa, S. Hitomi, R. Okuyama, R. Usui, Y. Yamada and S. Komaba, *Nature mater.*, 2012, **11**, 512-517.
54 W. M. Dose, N. Sharma, J. C. Pramudita, J. A. Kimpton, E. Gonzalo, M. H. Han and T. Rojo, *Chem. Mater.*, 2016, **28**, 6342-6354.
55 J. Thorne, R. Dunlap and M. Obrovac, *J. Electrochem. Soc.*, 2013, **160**, A361-A367.
56 B. Mortemard de Boisse, D. Carlier, M. Guignard, L. Bourgeois and C. Delmas, *Inorg. Chem.*, 2014, **53**, 11197-11205.
57 X. Ma, H. Chen and G. Ceder, Electrochemical properties of monoclinic $NaMnO_2$, *J. Electrochem. Soc.*, 2011, **158**, A1307-A1312.
58 T. Ohzuku, A. Ueda, N. Yamamoto, *J. Electrochem. Soc.*, 1995, **142**, 1431-1435.
59 Y. You, X. L. Wu, Y. X. Yin and Y. G. Guo, *J. Mater. Chem. A*, 2013, **1**, 14061-14065.
60 K. Du, J. Zhu, G. Hu, H. Gao, Y. Li and J. B. Goodenough, *Energy Environ. Sci.*, 2016, **9**, 2575-2577.
61 G. G. Amatucci, N. Pereira, T. Zheng, I. Plitz and J. M. Tarascon, *J. Power Sources*, 1999, **81**, 39-44.
62 T. Muraliganth, K. R. Stroukoff and A. Manthiram, Chem. Mater., 2010, **22**, 5754-5761.
63 Y. S. Lee and M. Yoshio, *Electrochem. Solid State Lett.*, 2001, **4**, A155-A158.
64 Y. Terada, Y. Nishiwaki, I. Nakai and F. Nishikawa, *J. Power Sources*, 2001, **97**, 420-422.
65 T. Aoshima, K. Okahara, C. Kiyohara and K. Shizuka, *J. Power Sources*, 2001, **97**, 377-380.
66 S. M. Oh, S. W. Oh, C. S. Yoon, B. Scrosati, K. Amine and Y. K. Sun, *Adv. Funct. Mater.*, 2010, **20**, 3260-3265.
67 M. Sathiya, G. Rousse, K. Ramesha, C. P. Laisa, H. Vezin, M. T. Sougrati, M. L. Doublet, D. Foix, D. Gonbeau, W. Walker, A. S. Prakash, M. Ben Hassine, L. Dupont and J. M. Tarascon, *Nature Mater.*, 2013, **12**, 827-835.
68 P. E. Pearce, A. J. Perez, G. Rousse, M. Saubanere, D. Batuk, D. Foix, E. McCalla, A. M.Abakumov, G. Van Tendeloo, M.-L. Doublet and J.-M. Tarascon, *Nature Mater.*, 2017, **16**, 850-856.